Journal of Manufacturing Science and Engineering

Technical Briefs

Point Laser Triangulation Probe Calibration for Coordinate Metrology

Kevin B. Smith
Assistant Professor, Brigham Young University, Department of Electrical and Computer Engineering, Provo, UT 84602

Yuan F. Zheng
Professor, The Ohio State University, Department of Electrical Engineering, Columbus, OH 43210

Point Laser Triangulation (PLT) probes have significant advantages over traditional touch probes. These advantages include throughput and no contact force, which motivate use of PLT probes on Coordinate Measuring Machines (CMMs). This document addresses the problem of extrinsic calibration. We present a precise technique for calibrating a PLT probe to a CMM. This new method uses known information from a localized polyhedron and measurements taken on the polyhedron by the PLT probe to determine the calibration parameters. With increasing interest in applying PLT probes for point measurements in coordinate metrology, such a calibration method is needed.
[S1087-1357(00)01703-2]

1 Introduction

Point Laser Triangulation (PLT) probes have a number of significant advantages over touch trigger and contact scanning probes that make them very useful in coordinate metrology. Some main advantages include zero contact force, small foot print, large range of allowable stand-off distances, and high bandwidth.

To apply Point Laser Triangulation (PLT) probes to coordinate metrology, the probes must be calibrated using a fast, readily automated, and accurate method to meet the needs of the industry. Existing calibration methods for CMM probes, such as touch trigger and contact scanning probes, are not adequate for calibrating PLT probes. Unlike other probes, the extrinsic calibration of PLT probes requires the additional parameters of an approach vector and an orientation vector as well as a translational vector. Current approaches do not model the added information provided by PLT probes, nor do they address the probe's unique operating constraints, such as sensor-to-surface orientation.

Much important work has been done in the calibration of positioning systems and sensors. Research in the calibration of positioning systems extends to applications in robotics [1–3], CNC machines tools [4–6], and Coordinate Measurement Machines [7]. Issues dealing with the intrinsic calibration of a noncontact LIDAR system [8] and the extrinsic calibration of noncontact sensors (i.e., cameras and laser line scanners) for integration on robots [9,10] and CMMs [11] have also been studied. As in our approach, these calibration methods primarily use parameter estimation techniques.

The extrinsic calibration of a noncontact ''light-striping'' probe on a CMM is presented in [12]. The modeling is based on a skewed frame representation, and the unknowns are solved for by minimizing an augmented objective function. The technology of a light-striping probe is very similar to that of a PLT probe; however, the light-striping probe produces 2D data points rather that 1D and therefore uses different calibration parameters.

One extrinsic calibration method for PLT probes on CMMs proposed to date [13] uses crosshairs to visually position the PLT probe laser beam to known coordinates. The disadvantages of this method are that 1) the calibration process cannot be automated, 2) the accuracy of the calibration is a function of the skill of the operator, and 3) the accuracy of the calibration parameters is lower than the accuracy of the PLT probe displacement measurement.

Our proposed calibration method overcomes these disadvantages. This method can be readily automated. Its accuracy is independent of operator skill level, and it yields accurate calibration parameters. The basic ideas for this method are extensions of the parameter estimation methods cited above and of part localization, [14,15].

In our approach, a calibration artifact is used that has a known geometry and is localized (i.e., the artifact's local reference frame is known relative to the CMM reference frame). The artifact (a polyhedron) is measured with the PLT probe mounted on and translated by the CMM. By fitting the measured points to known information, the calibration parameters can be estimated.

The rest of the paper is organized as follows. The calibration parameters of a touch probe are presented and then compared with the calibration parameters of a PLT probe. The proposed calibration method is then presented, along with the least squares solution. The approach is then analyzed from a sensitivity study, using the condition number to determine optimal configurations for the artifact, probe orientation, and number and location of points to measure. A simulation analysis is used to confirm the analysis. Finally, the effectiveness of the calibration is verified by use of comparative analysis.

2 Touch Probe Calibration Parameters

The calibration parameters of a touch probe include a tip sphere radius, r_T, and a translational vector, $\mathbf{t}_T$, that extends from the CMM quill to the center of the touch probe tip (see Fig. 1). When a part is measured with a touch probe, the probe tip is moved to contact the workpiece surface. At this contact location, the CMM quill position, $\mathbf{P}_q$, is determined from the *x*, *y*, *z* linear scales of the CMM. The point, P_T, on the workpiece at which the probe tip makes contact is given by

Contributed by the Manufacturing Engineering Division for publication in the JOURNAL OF MANUFACTURING SCIENCE AND ENGINEERING. Manuscript received April 1997; revised Oct. 1999. Associate Technical Editor: C. H. Menq.

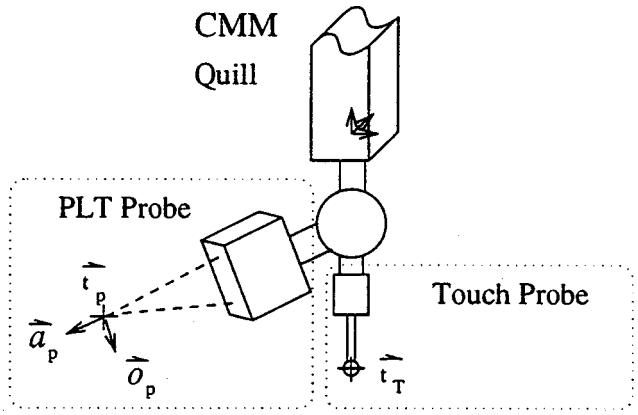

Fig. 1 The calibration parameters for a touch probe include a translational vector, $\mathbf{t}_T$, and tip radius, r_T. The calibration parameters for a PLT probe include a translational vector, $\mathbf{t}_p$, an approach vector, $\mathbf{a}_p$, and an orientation vector, o.

$$\mathbf{P}_T = \mathbf{P}_q + \mathbf{t}_T - r_T \mathbf{n}_w, \tag{1}$$

where $\mathbf{n}_w$ is the normal to the workpiece surface at the point of contact.

3 PLT Probe Calibration Parameters

A PLT probe has two additional calibration parameter vectors not required by a touch probe. The calibration parameters of a PLT probe include a translational vector, $\mathbf{t}_p$, an approach vector, $\mathbf{a}_p$, and an orientation vector, $\mathbf{o}_p$.

The translational vector, $\mathbf{t}_p$, is defined from a known location on the CMM quill (typically the center of a previously calibrated touch probe) to a reference position on the laser beam of the PLT probe. The approach vector, $\mathbf{a}_p$, is parallel to the laser beam and points toward the workpiece away from the PLT probe. The orientation vector, $\mathbf{o}_p$, is perpendicular to the laser beam and is directed from the laser beam toward the optical axis of the receiving lens.

An absolute position point, $\mathbf{P}_p$, on the workpiece is calculated from the PLT probe's measured displacement value, γ, and other calibration parameters by

$$\mathbf{P}_p = \mathbf{P}_q + \mathbf{t}_p + \gamma \mathbf{a}_p. \tag{2}$$

The orientation vector, **o**, is not used in this calculation, but is needed in path-planning algorithms to optimize sensor-to-surface orientations and to operate in collision-free regions. Since the orientation vector does not directly affect the accuracy of the PLT probe measurement, it can be approximated by visual inspection and is not part of the method presented here.

4 Proposed Calibration Method

The main steps in the proposed PLT probe calibration method are to 1) localize and calibrate the polyhedron artifact; 2) measure the facets of the polyhedron by recording the PLT probe's displacement value, γ_{ij}, and the CMM's position, $\mathbf{P}_q$, at each measurement; and 3) find the PLT probe calibration parameters that best fit the measurements to the polyhedron.

For this calibration method, a polyhedron with three facets is recommended for the artifact; although, more facets can be used (see Fig. 2). The polyhedron's m facets, $S_j(\mathbf{n},d)$, $j=1,\ldots,m$ are defined by their corresponding normals, $\mathbf{n}_j$, and minimum distances, d_j, from the origin (as referenced by the CMM) to the facet.

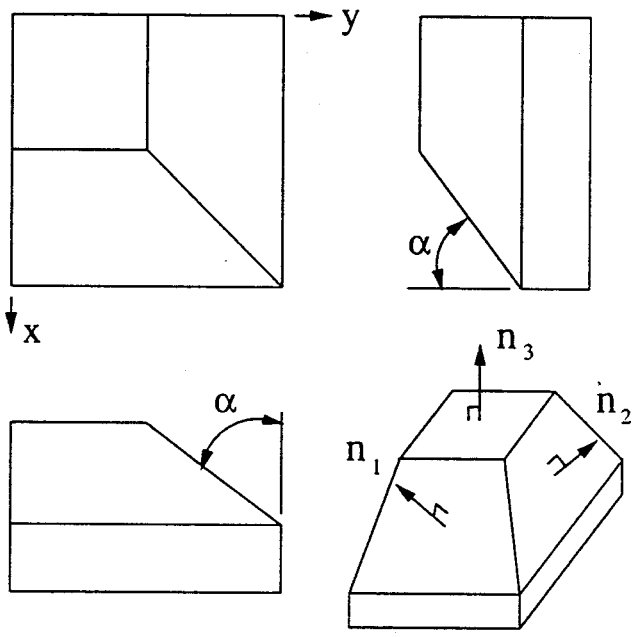

Fig. 2 A polyhedron with three facets is proposed as the calibration artifact

5 Deriving the Calibration Parameters

The measurement error (or residual), δ_{ij}, of the ith point normal to the facet is given by

$$\delta_{ij} = \mathbf{n}_j \cdot \mathbf{P}_{ij} - d_j, \tag{3}$$

$$= \mathbf{n}_j \cdot (\mathbf{P}_{qij} + \mathbf{t}_p + \gamma_{ij}\mathbf{a}_p) - d_j. \tag{4}$$

By construction, the only unknowns in Eq. (4) are $\mathbf{t}_p$, and $\mathbf{a}_p$. Since the equation is linear in unknowns, they can be solved for using the following simple linear least squares approach. Let f be the sum of the square of all the residuals, that is, $f = \sum_{j=1}^{m}\sum_{i=1}^{k_j}\delta_{ij}^2$, where k_j is the number of measured points on facet j. The calibration parameters can then be determined by finding values for **a** and **t** that minimize f. The function f is a minimum when the partials of f with respect to the unknowns $\{a_x, a_y, a_z, t_x, t_y, t_z\}$ are all equal to zero. Writing this system in matrix notation with $h=[a_x, a_y, a_z, t_x, t_y, t_z]^T$ results in

$$Gh = B, \tag{5}$$

where

$$G(\mathbf{n}_j, \gamma_{ij}) = \sum_{j=1}^{m}\sum_{i=1}^{k_j} g_{ij}, \tag{6}$$

$$g_{ij} = M_{ij} V [1]_{6x6} V M_{ij}, \tag{7}$$

$$B(\mathbf{n}_j, d_j, P_{qij}, \gamma_{ij}) = \sum_{j=1}^{m}\sum_{i=1}^{k_j} b_{ij}, \tag{8}$$

$$b_{ij} = M_{ij}[n_{xj}, n_{yj}, n_{zj}, n_{xj}, n_{yj}, n_{zj}]^T (d_j - \mathbf{n}_j \cdot \mathbf{P}_{qij}). \tag{9}$$

The 6×6 matrix, M_{ij}, has $\{\gamma_{ij}, \gamma_{ij}, \gamma_{ij}, 1, 1, 1\}$ on the main diagonal and 0 elsewhere. The 6×6 matrix V has $\{n_{xj}, n_{yj}, n_{zj}, n_{xj}, n_{yj}, n_{zj}\}$ on the main diagonal and 0 elsewhere. The 6×6 matrix, $[1]_{6x6}$, has all elements equal to 1.

As shown, the calibration parameters can be determined by solving Eq. (5) which is linear. The matrix G is called the displacement matrix because it is a function of the displacement measurements. The conditions for which a solution exists (i.e., G is invertible) will now be examined.

6 Constraints from the Displacement Matrix

A constraint on the displacement measurements and the facet normals is found by examining the conditions needed for the displacement matrix to be invertible. Carrying out the second sum in Eq. (6) and applying elementary row operations the top three rows can be written in the form

$$kn_x n_y n_z[\tau n_x \;\; \tau n_y \;\; \tau n_z \;\; \rho n_x \;\; \rho n_y \;\; \rho n_z]_j, \tag{10}$$

and the bottom three rows can be written in the form

$$\rho n_x n_y n_z[\rho n_x \;\; \rho n_y \;\; \rho n_z \;\; kn_x \;\; kn_y \;\; kn_z]_j \tag{11}$$

where

$$\tau_j = \sum_{i=1}^{k_j} \gamma_{ij}^2, \tag{12}$$

$$\rho_j = \sum_{i=1}^{k_j} \gamma_{ij}. \tag{13}$$

Thus the rank of D_j is

$$\text{rank}(D_j) = \begin{cases} 1, & \text{if } k_j\tau_j = \rho_j^2 \\ 2, & \text{if } k_j\tau_j \neq \rho_j^2. \end{cases} \tag{14}$$

From this information, the rank of G is bounded by

$$\text{rank}(G) = \text{rank}\left(\sum_{j=1}^{m} D_j\right) \leqslant \min\left(6, \sum_{j=1}^{m} \text{rank}(D_j)\right). \tag{15}$$

Using only three facets (i.e., $m=3$) requires that the rank of $D_1 = D_2 = D_3 = 2$ (i.e., requiring that $k_j\tau_j \neq \rho_j^2$). Conversely, if $k_j\tau_j = \rho_j^2$, more than three facets (i.e., $m \geqslant 6$) are required for G to be full rank.

In addition, if $\gamma_{ij} = C_j$ for all i, where C_j is a constant, then from Eqs. (12) and (13), $\tau_j = k_j C_j^2$ and $\rho_j = k_j C_j$. Under this condition, $k_j\tau_j = \rho_j^2$ and the rank of D_j is 1. Also, if $m=3$, then G is not invertible. As a practical consequence, the PLT probe must be positioned so that γ_{ij} is not constant while a facet is being measured.

Further, the $\text{rank}(D_1 + D_2 + D_3) = 6$ requires that the $\text{rank}(\mathbf{n}_1, \mathbf{n}_2, \mathbf{n}_3) = 3$ (i.e., the facet normals must be linearly independent).

In summary, the sufficient constraints from the displacement matrix are as follows: 1) at least three facets that have linearly independent normal vectors must be used, 2) each facet must be measured at least twice, and 3) the displacement values measured on a single facet cannot all be the same.

7 Calibration Parameter Sensitivity

For the calibration parameters, $\mathbf{a}_p$ and $\mathbf{t}_p$, to be determined accurately, they need to be sensitive to the PLT probe displacement measurement and the CMM quill position which improves the accuracy of the calibration while the effects of random noise errors can be minimized.

The calibration parameters are determined by minimizing the residuals in Eq. (4). The sensitivity of these residuals to the PLT probe measurement is given by

$$\left|\frac{\partial \delta_{ij}}{\partial \gamma_{ij}}\right| = |\mathbf{n}_j \cdot \mathbf{a}_p| \leqslant 1. \tag{16}$$

This sensitivity increases as the angle between the approach vector, $\mathbf{a}_p$, and the facet normal, $\mathbf{n}$, approaches 180 deg. Therefore, the facet normals should be aligned as close as possible to the PLT approach vector.

The sensitivity of residuals, δ_{ij}, to the CMM quill position, $\mathbf{P}_{qij}$, is given by

$$\frac{\partial \delta_{ij}}{\partial P_{xqij}} = n_x, \tag{17}$$

$$\frac{\partial \delta_{ij}}{\partial P_{yqij}} = n_y, \tag{18}$$

$$\frac{\partial \delta_{ij}}{\partial P_{zqij}} = n_z. \tag{19}$$

Equations (18) and (19) show that the sensitivity of the residuals to changes in CMM quill position along an axis is equal to the coordinate value of the facet normal vector in that axis. Therefore, the facet unit normal should ideally point along the CMM axis that has the highest resolution. However, if all three of the CMM axes have equal linear resolutions then the facet normal can point in any direction without changing the sensitivity of the residuals to CMM position changes.

8 Condition Number Analysis

The sensitivity of parameter errors, δh, resulting from the errors δG and δB in G and B respectively are characterized by the well-known condition number, $\kappa(G)$. This number is defined as $\kappa(G) \equiv \|G\| \, \|G^{-1}\| \geqslant 1$. In our application, a small condition number corresponds to the solution being less sensitive to data error.

By examining, G, one finds that the four parameters which affect the condition number include: 1) the number of measurements taken on each facet, K_j, 2) the threshold value of γ_{ij}, 3) the range value of γ_{ij}, and 4) the facet angle, α.

To reduce the condition number as much as possible, one has to make an effort to optimize the following items: 1) the number of measurements taken on each facet should be as large as realistically possible, 2) the threshold value of γ_{ij} should be set small because a large threshold value will result in a large condition number, and 3) the facet angle should be close to zero.

While it is feasible to achieve item 1) and 2), item 3) cannot be fully optimized because of limitations on allowable sensor-to-surface orientations. So a trade-off between the magnitude of $\kappa(G)$ and the expected accuracy of the PLT probe must be made.

To address this trade-off, PLT probe manufacturers specify a maximum allowable approach angle, $\theta_{\max}$. The approach angle is calculated from $\theta = \cos^{-1}(\mathbf{n}_j \cdot (-\mathbf{a}))$ and must be less than or equal to $\theta_{\max}$ for the PLT probe to meet its performance specifications. The smallest block angle, $\alpha_{\min}$, possible under this constraint is realized when the calibration artifact is positioned so that the approach angle is the same for all facets. Using plane geometry, this angle is given by $\alpha_{\min} = \tan^{-1}(\tan(\phi_t)/\sqrt{2})$, where $\phi_t = \cos^{-1}(-\cos(\theta_{\max})/\sqrt{2}) - \theta_{\max} + \pi/2$.

9 Calibration Experiment

An experiment was designed and conducted to validate the proposed PLT probe calibration method.

The main steps in the validation process are as follows: 1) calibrate a CMM touch probe; 2) secure the polyhedron artifact in the working zone of the CMM; 3) use the touch probe to localize and calibrate the polyhedron artifact; 4) calibrate the PLT probe using the proposed calibration method; 5) move the artifact to a new location in the CMM working zone, change its orientation, and secure its position; 6) measure the artifact facets at the new location with the PLT probe; 7) install and calibrate the touch probe; 8) measure the artifact with the touch probe in its new location; and 9) compare the facet normals and minimum distances obtained from the PLT probe with those obtained from the touch probe.

The parameters $\mathbf{n}_j$ and d_j were obtained using the CMM's standard plane measuring and datuming routines for touch probe measurements. The displacement measurements, γ_{ij}, and the corresponding CMM quill positions, $\mathbf{P}_{qij}$, were obtained while measuring the facets with the PLT probe.

Table 1 Performance of touch probe and two PLT probes

Probe	ROR (μm)	SDR (μm)	ABL ($arcmin$)
Touch	2.4	0.53	-0.16
PLT_A	485	80	32.7
PLT_B	11	2.18	0.44

Table 2 The angle between the facet normal n_{ideal} and n, where n_{ideal} was measured by the touch probe and n was measured by the PLT probe.

probe	Facet#1	Facet#2	Facet#3
	(10^{-3}) radians	(10^{-3}) radians	(10^{-3}) radians
PLT_A	0.76	3.21	1.07
PLT_B	0.37	0.34	0.41

Table 3 The difference between the minimum facet distance to the origin determined by the touch probe and by the PLT probe

Probe	Facet#1	Facet#2	Facet#3
PLT_A	3.328 mm	-0.203 mm	3.296 mm
PLT_B	-0.006 mm	-0.013 mm	-0.021 mm

A method for determining the facet normal vectors, $\mathbf{n}_{pj}$, and corresponding minimum distances, d_{pj}, measured by the PLT probe in the ''moved'' validation position (step #5) needed to be developed. Since the calibration parameters were previously determined, a point, $\mathbf{P}_{pij}$, measured by the PLT probe is determined from Eq. (2). The relationship between $\mathbf{n}_{pj}$, d_{pj}, and $\mathbf{P}_{pij}$ is given by

$$\mathbf{P}_{pij} \cdot \mathbf{n}_{pj} = d_{pj}. \tag{20}$$

Using the change of variable, $\boldsymbol{\lambda}_{pj} = 1/d_{pj}\mathbf{n}_{pj}$, and letting the matrix Z be defined as

$$Z_j = \begin{bmatrix} P_{xp1} & P_{yp1} & P_{zp1} \\ P_{xp2} & P_{yp2} & P_{zp2} \\ & \vdots & \\ P_{xp16} & P_{yp16} & P_{zp16} \end{bmatrix}_j, \tag{21}$$

the system of equations for the points measured on a facet in matrix form is

$$Z_j \boldsymbol{\lambda}_{pj} = [1]_{16\times 1}. \tag{22}$$

This least squares problem has the unique solution

$$\boldsymbol{\lambda}_{pj} = (Z_j^T Z_j)^{-1} Z^T [1]_{16\times 1}. \tag{23}$$

Finally, the desired parameters can be determined from $\boldsymbol{\lambda}_{pj}$ by

Table 4 The range of minimum distance residuals from the PLT probe measurements

Probe	Facet#1	Facet#2	Facet#3
PLT_A	0.119 mm	0.401 mm	0.133 mm
PLT_B	0.019 mm	0.010 mm	0.018 mm
Touch	0.005 mm	0.006 mm	0.007 mm

$$\mathbf{n}_{pj} = \frac{\boldsymbol{\lambda}_{pj}}{\|\boldsymbol{\lambda}_{pj}\|} \tag{24}$$

and

$$d_{pj} = \frac{1}{\|\boldsymbol{\lambda}_{pj}\|}. \tag{25}$$

For purposes of comparison, the validation experiment was performed using two commercially available PLT probes referenced as PLT_A and PLT_B in this document. The CMM used to calibrate the PLT probes was a Sheffield RS-30. The touch probe used was a Renishaw TP-2 touch probe with a 1 mm tip diameter. The polyhedron artifact with three facets, depicted in Fig. 2, was manufactured from an aluminum block with a facet angle of $\alpha = 60$ deg.

To quantify the performance of the touch probe and two PLT probes independent of the calibration method, a 5-arcmin angle block was measured. In this test, the probes were mounted vertically and the block was measured 100 times at evenly spaced intervals over a length of 20 mm. A line was fit to the measured points; and the following were calculated: the range of residuals (ROR), the standard deviation of the residuals (SDR), and angle between theoretical line and fitted line (ABL). The results are shown in Table 1.

In this experiment, the touch probe performed significantly better than both laser probes. These probes were then used in the validation experiment explained above; the results are shown in Tables 2, 3, and 4.

Table 2 reports the angle, ϵ_n, between the facet normal $\mathbf{n}_{\text{ideal}}$, measured by the touch probe, and $\mathbf{n}_p$, measured by the PLT probe. The angle, ϵ_n, is calculated by

$$\epsilon_n = \cos^{-1}(\mathbf{n}_p \cdot \mathbf{n}_{\text{ideal}}). \tag{26}$$

Table 3 reports the difference, ϵ_d, between the minimum distance from the facet to the origin determined by the touch probe, $d_{j,\text{ideal}}$, and by the PLT probe, d_{pj}; that is,

$$\epsilon_d = d_{j,\text{ideal}} - d_{pj}. \tag{27}$$

Table 4 reports the range, ϵ_r, of the difference between the least-squares minimum facet distance, d_{pj}, and the minimum facet distance calculated from individual facet points measured by the PLT probe. That is,

$$\epsilon_r = \text{range}(d_j - d_{pij})_j \quad i = 1,2,\ldots,16. \tag{28}$$

The variation in experimental results between the two PLT probes tested is consistent with the measurement accuracy of the respective PLT probes. The validation experiment results confirm the high accuracy of this proposed PLT probe calibration method.

10 Summary

The proposed PLT probe calibration method is an accurate calibration method that can execute autonomously and provide a linear solution. A mathematical and experimental analysis of the proposed calibration method revealed the following design constraints.

1 The condition number, $\kappa(G)$, should be small.
2 The polyhedron should be positioned during the calibration so that the angle between the facet normal vectors and the PLT laser beam is as small as possible.
3 Certain conditions must be satisfied for the inverse of the displacement matrix, G^{-1}, to exist:

- At least three facets must be measured.
- The facet normal vectors must span $\mathcal{R}^3$ (i.e., Rank($\{\mathbf{n}_1, \mathbf{n}_2, \ldots, \mathbf{n}_m\}$)$=3$).
- When only three facets are measured, at least two measurements per facet must be taken (i.e., $k_j \geqslant 2$ for $j=1,2,\ldots,m$ where $m=3$).
- The PLT probe displacement values must be controlled, as shown in Eq. (14).

This proposed calibration method was validated experimentally to provide an accurate coordinate calibration for a PLT probe. The accuracy of the calibration is limited principally by the accuracy of the PLT probe.

Acknowledgments

This research was funded in part by the Engineering Research Center for Net Shape Manufacturing (ERC/NSM) at The Ohio State University, by the Office of Naval Research under grant N00014-90-J-1516, and by the National Institute of Standards and Technology (NIST), an agency of the U.S. Department of Commerce.

References

[1] Hayati, S. A., 1983, ''Robot arm geometric link parameter estimation,'' *22nd IEEE Control System Society Conference on Decision and Control* (San Antonio, Texas), Vol. 3, No. 7, pp. 1477–1483.
[2] Menq, C. H., and Borm, J. H., 1988, ''Estimation and observability measure of parameter errors in a robot kinematic model,'' *Proceedings of U.S.A.-Japan Symposium on Flexible Automation* (Minneapolis, July 18–20), pp. 65–70.
[3] Borm, J. H., and Menq, C. H., 1991, ''Determination of optimal measurement configurations for robot calibration based on observability measure,'' Int. J. Robot. Res., **10**, No. 1, pp. 51–63.
[4] Hocken, R. J., 1980, ''Technology of machine tools, Vol. 5, Machine tool accuracy,'' *Machine Tool Task Force*.
[5] Ni, J., 1997, ''CNC machine accuracy enhancement through real-time error compensation,'' Trans. ASME, J. Manuf. Sci. Eng., **119**, pp. 717–725.
[6] Lee, E. S., Suh, S. H., and Shon, J. W., 1998, ''Comprehensive method for the calibration of volumetric positioning accuracy of CNC-machines,'' Int. J. Adv. Manufac. Technol. (Springer-Verlag London Ltd., London Engl.), **119**, No. 1, pp. 43–49.
[7] Chen, J., and Chen, Y. F., 1987, ''Estimation of coordinate measuring machine error parameters,'' *Proceedings of IEEE International Conference on Robotics and Automation* (San Francisco), pp. 1011–1016, Apr. 7–10.
[8] Chen, Y. D., and Ni, J., 1993, ''Dynamic calibration and compensation of a 3-D laser radar scanning system,'' IEEE Trans. Rob. Autom., **9**, No. 3, pp. 318–322.
[9] Agin, G. J., 1985, ''Calibration and use of a light stripe range sensor mounted on the hand of a robot,'' *Proceedings of the IEEE International Conference on Robotics and Automation*, St. Louis.
[10] Chen, C., H., and Kak, A. C., 1987, ''Modeling and calibration of a structured light scanner for 3-D robot vision,'' *Proceedings of the 1987 IEEE International Conference on Robotics and Automation*, CH2413-3., pp. 807–815.
[11] Agin, G. J., and Highnam, P. T., 1987, ''Movable light-strip sensor for obtaining three-dimensional coordinate measurement,'' *Proceedings of the SPIE International Tech. Sym.*, San Diego, CA, pp. 326–333, Aug. 21–27.
[12] Che, C., and Ni, J., 1996, ''Modeling and calibration of a structured-light optical CMM via skewed frame representation,'' Trans. ASME, J. Manufact. Sci. Eng., **118**, pp. 595–603.
[13] Hu, W. 1995, ''3-D surface digitizing using coordinate measuring machines (CMM) with laser displacement sensors (LDS),'' Master's thesis, Dept. of Electrical Engineering, The Ohio State University.
[14] Sahoo, K. C., and Menq, C. H., 1991, ''Localization of 3-D objects having complex sculptured surfaces using tactile sensing and surface description,'' ASME J. Eng. Ind., **523**, pp. 85–92.
[15] Gunnarsson, K. T., and Prinz, F. B., 1987, ''CAD model-based localization of parts in manufacturing,'' IEEE Comput., **20**, pp. 66–74.

Simultaneous Optimization of Machining Parameters for Dimensional Instability Control in Aero Gas Turbine Components Made of Inconel 718 Alloy

B. K. Subhas
Scientist F

Ramaraja Bhat
Scientist B

K. Ramachandra
Scientist G

Gas Turbine Research Establishment, Bangalore, India-560 093
e-mail: gtre@vigyan.iisc.ernet.in

H. K. Balakrishna
Dean,
Sir M. Visvesvarayya Institute of Technology, Bangalore, India-562 157

Aero gas turbine components made of Inconel 718 superalloy revealed significant dimensional instability after machining. The dimensional instability is a manifestation of alterations in residual stresses and microstructure, which are influenced by machining parameters. This paper presents a simultaneous optimization technique used to control the dimensional instability in turning operation. Empirical equations are established for predicting surface residual stresses, surface finish, dimensional instability and tool life using response surface methodology. Experimental results show a strong correlation between residual stresses and dimensional instability. A desirability function approach is used to optimize the multiple responses and machining parameters are derived for practical applications. Inconel 718 test specimen and jet engine components machined with optimal cutting parameters show dimensional instability within the acceptable tolerance band. [S1087-1357(00)01704-4]

1 Introduction

Modern aero gas turbine engine components are complex in their shape, thin walled and call for very close dimensional tolerances and good surface integrity. Inconel 718 superalloy is extensively used for jet engine components. This nickel-based superalloy is not only difficult to machine but also revealed dimensional instability after machining. The dimensional instability is a change in dimension with respect to time without doing any further work on the component [1]. The dimensional instability of components poses problems during assembly. Residual stresses and microstructure changes in a machined surface region cause dimensional instability [1]. Dimensional instability can be controlled by selection of proper machining parameters that influence the residual stresses and microstructure changes in a machined

Contributed by the Manufacturing Engineering Division for publication in the JOURNAL OF MANUFACTURING SCIENCE AND ENGINEERING. Manuscript received Oct. 1997; revised Feb. 2000. Associate Technical Editor: K. Sutherland.

surface region. The selection of machining parameters also depends on other responses such as required tool life, surface finish, material removal rate, etc. Therefore, the machining operation has to be optimized considering several process responses.

Derringer and Suich [2] presented a problem involving simultaneous optimization of several response functions that depend upon the number of process variables. This approach is based on transforming response variables into desirability functions [3], which can be optimized by univariable techniques. The desirability function is a dimensionless number, varying between ''0'' for completely undesirable level and ''1'' for completely acceptable level of process quality. The geometric mean of desirabilities for several responses is a dimensionless number that represents overall quality of the process. Thus, optimization problems are reduced to problems of optimizing single function. That is, overall desirability has to be optimized with respect to process variables. This paper presents a desirability function approach for simultaneous optimization of turning operations. Empirical equations are developed for predicting responses by response surface methodology [4]. Response surface methodology involves statistical design of experiments that reduce the number of experiments required. The prediction equations for the responses are derived in terms of independent machining parameters by regression analysis.

In this paper, dimensional instability of machined component, tool life, surface finish and material removal rate are considered for optimizing turning parameters. The validity of optimal machining parameters to control the dimensional instability is experimentally verified on test specimens and actual gas turbine engine components.

2 Methodology

The steps involved in the proposed methodology are:

(i) Selection of process variables and responses.
(ii) Design of statistical experiment.
(iii) To determine empirical equations for predicting responses by response surface methodology and check the adequacy of equations.
(iv) To compute optimal machining parameters using desirability function approach.

2.1 Selection of Process Variables and Responses. The optimization technique is developed here for a turning operation since most of the critical rotating gas turbine components are machined by turning. Speed, feed, depth of cut, tool rake angle and tool nose radius are the variables that significantly affect residual stresses and microstructure in a machined surface region [5]. Soluble oil (1:20) cutting fluid and micrograin grade carbide (Kennametal K68) cutting tool material were selected based on earlier experimental investigation [6]. Table 1 shows the maximum and minimum values of cutting parameters used in experiments.

Considering the surface integrity and accuracy requirement of precision rotating gas turbine components and efficiency of turning operation, optimization is done for six process responses, namely, circumferential and longitudinal residual stresses, dimensional instability, surface finish, tool life and material removal rate. Therefore, empirical equations are developed for these six responses. The material removal rate is calculated using,

Table 1 Cutting parameters used for machining

Process Variables	Maximum (+)	Minimum (-)
v	38	10
f	0.22	0.04
d	1.0	0.25
α	+6	-6
r	1.2	0.4

Table 2 Treatment combinations of process variables

Trial No.	Process variables					Treatment effects
	v	f	d	α	r	
1	+	-	-	-	-	v
2	-	+	-	-	-	f
3	-	-	+	-	-	d
4	-	-	-	+	-	α
5	-	-	-	-	+	r
6	+	+	+	-	-	vfd
7	+	+	-	+	-	$vf\alpha$
8	+	-	+	+	-	$vd\alpha$
9	-	+	+	+	-	$fd\alpha$
10	+	+	-	-	+	vfr
11	+	-	+	-	+	vdr
12	+	-	-	+	+	$v\alpha r$
13	-	+	+	-	+	fdr
14	-	+	-	+	+	$f\alpha r$
15	-	-	+	+	+	$d\alpha r$
16	+	+	+	+	+	$vfd\alpha r$

$$MRR = 1000 \cdot v \cdot f \cdot d \tag{1}$$

The prediction equations for other five responses are determined by statistical design of experiment.

2.2 Statistical Design of Experiment. The influence of process variables on response functions was studied at two levels. A half replicate 2^5 factorial experiment was designed that involved only sixteen trials. The treatment combinations of five variables and corresponding experimental conditions are shown in Table 2 and Table 3. Error variances for the responses were estimated by carrying out four repeated experiments (Trial No. 17 to 20 in Table 3) at the central values of variables.

2.3 Experimental Procedure. Cylindrical test specimens (ID 55 mm×OD 76 mm×length 70 mm) made of Inconel 718 were stress relieved and aged (hardness 44 HRC). The specimen was held in a mandrel to avoid clamping pressure while turning. Turning trials were conducted in a HMT H-26 lathe (7.5 kW). The machined specimens were inspected at predetermined locations in a Zeiss Mauser 3D coordinate measuring machine. The dimensional instability was calculated as a maximum absolute difference between dimensions measured immediately after machining and final stable dimensions. Residual stresses were determined by hole drilling strain gage method [7]. The machining operation was interrupted periodically and tool flank wear was measured using a tool makers' microscope. Time taken to reach a value of 0.18 mm maximum flank wear was the criterion for tool life. Surface finish was measured using a portable perth-o-meter. Results of the experiments are given in Table 3.

Table 3 Experimental data

Trial No.	v	f	d	α	r	σ_c	σ_l	R_a	T	$DIMI$
1	38	0.04	0.25	-6	0.4	220.0	20.0	0.28	6.0	55.0
2	10	0.22	0.25	-6	0.4	350.0	31.5	2.40	6.5	87.5
3	10	0.04	1.0	-6	0.4	280.0	26.0	0.9	11.0	70.0
4	10	0.04	0.25	6	0.4	40.0	6.7	0.7	12.0	10.0
5	10	0.04	0.25	-6	1.2	130.4	19.0	0.3	12.5	50.0
6	38	0.22	1.0	-6	0.4	1010.3	62.8	1.8	5.0	205.0
7	38	0.22	0.25	6	0.4	611.5	43.5	0.8	6.0	191.0
8	38	0.04	1.0	6	0.4	212.5	16.7	0.9	7.5	38.0
9	10	0.22	1.0	6	0.4	319.8	24.9	3.2	8.0	63.0
10	38	0.22	0.25	-6	1.2	768.4	55.8	0.6	5.5	199.0
11	38	0.04	1.0	-6	1.2	371.6	29.0	0.7	7.0	78.0
12	38	0.04	0.25	6	1.2	172.8	15.5	0.6	8.5	43.0
13	10	0.22	1.0	-6	1.2	479.2	37.2	1.5	7.2	103.0
14	10	0.22	0.25	6	1.2	295.4	30.0	1.0	9.5	75.5
15	10	0.04	1.0	6	1.2	46.0	9.0	1.1	14.0	27.0
16	38	0.22	1.0	6	1.2	701.5	51.5	0.8	5.3	171.0
17	24	0.13	0.625	0	0.8	325.0	25.0	0.9	7.0	80.0
18	24	0.13	0.625	0	0.8	267.0	23.9	1.1	8.1	78.0
19	24	0.13	0.625	0	0.8	290.0	27.0	1.2	7.5	82.0
20	24	0.13	0.625	0	0.8	310.0	23.0	0.9	8.0	86.0

Table 4 Transformation equations for variables

Coded variable	Transformation equations
x_1	$\frac{2\nu - (\nu_{max} + \nu_{min})}{(\nu_{max} - \nu_{min})}$
x_2	$\frac{2f - (f_{max} + f_{min})}{(f_{max} - f_{min})}$
x_3	$\frac{2d - (d_{max} + d_{min})}{(d_{max} - d_{min})}$
x_4	$\frac{2\alpha - (\alpha_{max} + \alpha_{min})}{(\alpha_{max} - \alpha_{min})}$
x_5	$\frac{2r - (r_{max} + r_{min})}{(r_{max} - r_{min})}$

2.4 Equations for Predicting Process Responses. Following equation is postulated for the responses:

$$y = b_0 + \Sigma b_i x_i + \Sigma b_{ij} x_i x_j; \quad i,j = 1,2,3,4,5 \quad \text{and} \quad i \neq j \quad (2)$$

Equation (2) includes direct linear and interaction effects of the variables. For convenience, two levels of each independent variable are coded into -1(low) and $+1$(high). Transformation equations used for coding the variables are given in Table 4. The sixteen coefficients required for Eq. (2) were estimated by the method of least squares.

$$\{\mathbf{B}\} = (X'X)^{-1}X'\{\mathbf{Y}\} \quad (3)$$

where, X is the matrix of coded variables and $\{\mathbf{Y}\}$ is the vector of measured responses.

Predicting equations for all the responses are obtained in the form of Eq. (2), which involves sixteen terms. These equations were further simplified to include only statistically significant term of variables and their interactions [5]. The ratio of mean square effect to error variance was compared with F-statistics to test the significance of each effect at 95 percent confidence level. The prediction equations are thus simplified and involves fewer terms as follows:

$$\sigma_c = -138.6457 + 1.8569\nu + 643.4365f + 286.8036d - 2.3259\alpha + 109.2222r + 60.0156\nu f - 15.6297d\alpha - 174.7535dr \quad (4)$$

$$\sigma_l = 1.8836 + 0.0447\nu + 52.8845f + 13.2834d - 0.4828\alpha + 5.8073r + 3.4268\nu f - 0.6195d\alpha - 9.2915dr \quad (5)$$

$$T = 14.3911 - 0.2039\nu - 30.9241f + 0.1052\alpha + 1.1720r + 0.5473\nu f \quad (6)$$

$$DIMI = 8.9766 + 0.216\nu + 126.7825f + 33.5055d - 2.2595\alpha + 18.7364\nu f - 0.4259\nu d + 0.0302\nu\alpha - 122.2237fd + 4.7463f\alpha - 2.3614d\alpha \quad (7)$$

$$R_a = 1.0107 - 0.0172\nu + 8.8607f + 0.7035d - 0.0031\alpha - 1.2789r - 0.1766\nu f + 0.0246\nu r - 0.1874f\alpha \quad (8)$$

2.5 Adequacy of Prediction Equations. Equations (4)–(8) are valid when ν, f, d, α and r vary within the minimum and maximum levels used in the experiments (Table 1). Further, these equations were checked for adequacy by analysis of variance. The ratio of lack of fit mean square to pure error mean square is compared with F-statistic. The pure error mean square for the responses is estimated by repeated tests carried out at central values of the variables. The predicted equations are adequate since lack of fit is not significant at 95 percent confidence level (Table 5).

2.6 Correlation between Residual Stresses and Dimensional Instability. The coefficient of correlation between residual stresses and dimensional instability are calculated from the results of experiments presented in Table 3. The correlation coefficient between σ_c and $DIMI$ is 0.9602; σ_l and $DIMI$ is 0.9658—that is, residual stresses and dimensional instability are highly correlated, and by controlling dimensional instability residual stresses are also controlled. Therefore, the response functions, σ_c and σ_l are not considered for optimization.

2.7 Simultaneous Optimization. The machining process responses were transformed into desirability functions [2]. The desirability functions derived for the responses are given below:

$$d_1 = \begin{cases} 0 & T \leqslant T_{\min} \\ \left[\dfrac{T - T_{\min}}{T_{\max} - T_{\min}}\right] & T_{\min} < T < T_{\max} \\ 1 & T \geqslant T_{\max} \end{cases} \quad (9)$$

$$d_2 = \begin{cases} 0 & MRR \leqslant MRR_{\min} \\ \left[\dfrac{MRR - MRR_{\min}}{MRR_{\max} - MRR_{\min}}\right] & MRR_{\min} < MRR < MRR_{\max} \\ 1 & MRR \geqslant MRR_{\max} \end{cases} \quad (10)$$

$$d_3 = \begin{cases} 0 \quad DIMI < DIMI_{\min}, \ DIMI > DIMI_{\max} \\ \left[\dfrac{DIMI - DIMI_{\min}}{DIMI_c - DIMI_{\min}}\right] & DIMI_{\min} \leqslant DIMI \leqslant DIMI_c \\ \left[\dfrac{DIMI - DIMI_{\max}}{DIMI_c - DIMI_{\max}}\right] & DIMI_c \leqslant DIMI \leqslant DIMI_{\max} \end{cases} \quad (11)$$

Table 5 Analysis of variance for adequacy test

Response Variable	Source of variation	Sum of Squares	Degrees of Freedom	Mean Squares	F ratio computed	F-statistics (at 95%)
σ_c	(a) Lack of fit	28870.82	8	3608.85	5.70	8.85
	(b) Pure error	1898.0	3	632.67		
σ_l	(a) Lack of fit	138.54	8	17.32	5.83	8.85
	(b) Pure error	8.908	3	2.97		
T	(a) Lack of fit	4.6	11	0.418	1.63	8.77
	(b) Pure error	0.77	3	0.257		
$DIMI$	(a) Lack of fit	474.75	6	79.13	6.78	8.94
	(b) Pure error	35	3	11.67		
R_a	(a) Lack of fit	1.3325	8	0.167	7.40	8.85
	(b) Pure error	0.0675	3	0.0225		

Table 6 Optimal parameters

Tolerance Group	Independent parameters					Response parameters						Desirability				
	v	f	d	α	r	T	MRR	$DIMI$	R_a	σ_c*	σ_t*	d_1	d_2	d_3	d_4	D
Group II	10	0.04	0.5	6	1.2	13.4	200	15.75	0.254	39.3	9.2	0.558	0.037	0.848	0.909	0.355
Group III	16	0.05	0.6	6	1.2	12.1	480	24.98	0.432	79.3	11.2	0.471	0.139	0.995	0.614	0.447
Group IV	26	0.06	0.5	6	1.2	10.1	780	39.71	0.401	151.6	14.9	0.342	0.249	0.971	0.665	0.484

* Computed by substituting optimal independent parameters in equations (4) and (5).

$$d_4 = \begin{cases} 0 & R_a \geq R_{a\,\max} \\ \left[\dfrac{R_a - R_{a\,\max}}{R_{a\,\min} - R_{a\,\max}}\right] & R_{a\,\min} < R_a < R_{a\,\max} \\ 1 & R_a \leq R_{a\,\min} \end{cases} \quad (12)$$

One-sided transformation is used for the desirability of tool life, actual metal removal rate, surface finish; and two-sided transformation for dimensional instability. Overall (composite) desirability of the process is computed by geometric mean of individual desirabilities.

$$D = (d_1 \times d_2 \times d_3 \times d_4)^{1/4} \quad (13)$$

Maximizing this composite desirability gives the best overall performance for machining.

2.8 Optimization Criteria. In this study, tolerance bands for the jet engine components are classified into four groups.

Group No. I - 5–10 microns range
Group No. II - 11–20 microns range
Group No. III - 21–30 microns range
Group No. IV - 31–50 microns range

Only few components require 5–10 microns tolerance, which is achieved by either jig boring or grinding. Since the present study is limited only to turning operation, machining parameters are optimized for Group II to IV tolerance bands. Upper and lower limits of the tolerance group fix the maximum and minimum values for acceptable dimensional instability. The $DIMI_c$ is the mid-value of the tolerance band, where $d_3 = 1$. The constraints on tool life and surface finish are selected based on practical experience. $d_1 = 0$ at $T = 5$ min and $d_1 = 1$ at $T = 20$ min. Similarly, $d_4 = 0$ at $R_a = 0.8\,\mu$m and $d_4 = 1$ at $R_a = 0.2\,\mu$m, $MRR_{\min}$ and $MRR_{\max}$ were calculated as follows:

$$MRR_{\min} = 1000 \cdot \nu_{\min} \cdot f_{\min} \cdot d_{\min} \quad (14)$$

$$MRR_{\max} = \frac{P_m \cdot E}{1.25 \cdot p \cdot C_t \cdot C_r} \quad (15)$$

Following values were used in Eq. (15): P_m is 7500 W, p is 1.03 W/mm^3/min, E is 0.7, C_t and C_r are 1.2 [6]. With these constraints, desirabilities for the responses are computed by varying ν, f, d, α and r in discrete steps. A computer program is written for computing individual and composite desirabilities. The composite desirabilities for different combinations of process variables were numerically compared. The program prints optimal responses, variables and corresponding desirabilities upon reaching maximum value of D. Output of the computer program is summarized in Table 6.

3 Experimental Validation of Optimal Parameters

11–20 micron tolerance band is the most critical for turning operation. The validity of optimal machining parameters derived for this range are verified by carrying out tests on cylindrical test specimen and actual jet engine components.

3.1 Validation on Test Specimen. Table 7 shows dimensional details for the test specimen machined with $\nu = 10$ m/min, $f = 0.04$ mm/rev, $d = 0.5$ mm, $\alpha = 6$ deg and $r = 1.2$ mm. The changes in dimensions are less than 10 microns, which are well within the predicted value. Repeated tests carried out with these

Table 7 Dimensional instability in test specimen

Sl. No.	Specimen location	Immediately after machining (in mm)		After 360 hours (in mm)		Actual change in dimension (in mm)	
		Mean diameter	Roundness	Mean diameter	Roundness	Mean diameter	Roundness
1	ID at 5mm	60.5569	0.0145	60.5569	0.0137	no change	0.008
2	ID at 15mm	60.5634	0.02157	60.5630	0.0186	0.001	0.0029
3	OD at 5mm	66.3993	0.0151	66.3982	0.0136	0.0011	0.0015
4	OD at 15mm	66.3948	0.0125	66.3939	0.0118	0.009	0.007
5	OD at 25mm	66.3931	0.0117	66.3924	0.0094	0.007	0.0023

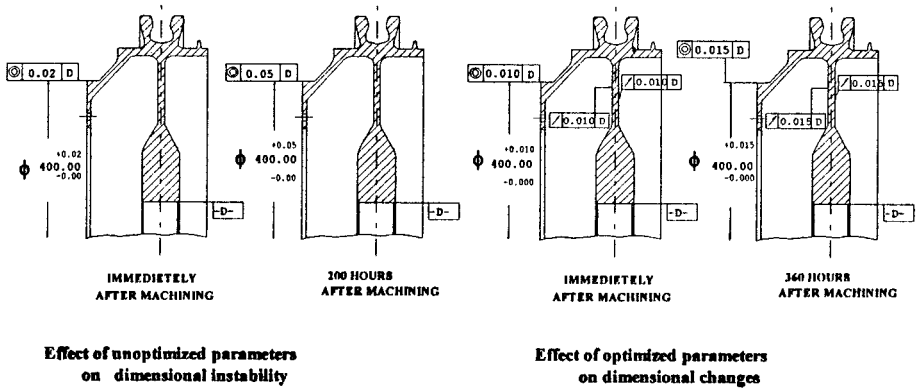

Fig. 1 Dimensional instability in compressor disc

machining parameters showed 5 percent scatter in dimensional instability, but all were within the required tolerance band.

3.2 Validation on Compressor Disc. Effect of optimal machining parameters on dimensional instability in compressor discs is shown in Fig. 1. The locating diameter 400 (+0.02/0.00) mm was machined using the optimal machining parameters derived for 11–20 micron tolerance group. The diameter maintained at 400 (+0.010/0.00) mm during machining has changed to 400 (+0.015/0.00) mm after 360 hours. This change in dimension is within the acceptable tolerance band.

4 Conclusion

1 Empirical equations for predicting surface residual stresses, dimensional instability, surface finish and tool life were derived by response surface methodology.

2 Experimental results have shown that residual stresses and dimensional instability are highly correlated. Therefore, dimensional instability, tool life, surface finish and material removal rate were considered for optimization.

3 A simultaneous optimization method based on desirability function approach was used. The optimal cutting parameters are derived to control dimensional instability within 11–20, 21–30 and 31–50 micron tolerance bands in turning precision aero gas turbine engine components made of Inconel 718.

4 Dimensional instability was within the acceptable tolerance band for the test specimen and actual jet engine components that are machined with optimal machining parameters obtained by simultaneous optimization.

Nomenclature

α = rake angle, deg.
b_i, b_{ij} = regression coefficients
$\{\mathbf{B}\}$ = vector of regression coefficients
C_r = rake angle correction factor
C_l = chip thickness correction factor
d = depth of cut, mm
d_1 = desirability of tool life
d_2 = desirability of material removal rate
d_3 = desirability of dimensional instability
d_4 = desirability of surface roughness
D = composite desirability
$DIMI$ = dimensional instability, μm
$DIMI_c$ = most desirable dimensional instability, μm
E = transmission efficiency of the drive
f = feed, mm/rev
ID = inner diameter, mm
MRR = metal removal rate, mm^3/min
OD = outer diameter, mm
p = power per unit metal removal rate, $W/mm^3/min$
P_m = lathe motor power, W
r = tool nose radius, mm
R_a = surface finish, μm
σ_c = circumferential residual stress MPa
σ_l = longitudinal residual stress MPa
T = tool life, min
ν = cutting speed, m/min
x_1 = coded value for ν
x_2 = coded value for f
x_3 = coded value for d
x_4 = coded value for α
x_5 = coded value for r
X = matrix of coded variables
X' = transpose of X
y = estimated response
$\{Y\}$ = vector of measured responses

Subscripts

max = indicates maximum value
min = indicates minimum value

References

[1] Marschall, C. W., and Maringer, R. E., 1977, ''Dimensional Instability-An introduction,'' *International Series of Material Science and Technology*, Pergamon Press, Vol. 22.
[2] Derringer, G., and Suich, R., 1980, ''Simultaneous Optimization of Several Response Variables,'' J. Quality Technol., **12**, No. 4, pp. 214–219.
[3] Harrington, Jr., E. C., 1965, ''The Desirability Function,'' Ind. Quality Control, pp. 494–498.
[4] Wu, S. M., 1964, ''Tool Life Testing by Response Surface Methodology, Part 1 and 2,'' ASME J. Eng. Ind., pp. 105–115.
[5] Devarajan, N. et al., 1984, ''Experimental Method of Predicting Residual Stress due to Turning in Stainless Steel,'' J. Exp. Tech., **8**, pp. 22–26.
[6] Subhas, B. K., 1983, ''Some Experimental Studies in Machining of Superalloys as Applied to Gas Turbine,'' M. S. Research thesis, J.N.T.U., Hyderabed.
[7] ''Measurement of Residual Stress by Hole Drilling Strain Gauge Method,'' 1993, Technical Note No. T.N.503-4, Measurement Group Inc.

Edge Radius Variability and Force Measurement Considerations

Roy J. Schimmel[1]
Graduate Research Assistant

Jairam Manjunathaiah[2]
Graduate Research Assistant

William J. Endres
Assistant Professor, Mem. ASME

Department of Mechanical Engineering and Applied Mechanics, University of Michigan, Ann Arbor, MI 48109

A new, noncontact instrument, based on white light interferometry, is used to measure the edge radii of cutting tools with measurement errors of less than 3 μm. Edges of several commercial cutting inserts are measured and compared. It is found that the radius of the hone varies along the length of the edge in a parabolic manner. The difference between the edge radius at the center of the edge and the radius at the start of the corner can be as large as 25 μm (0.001 in). The variation between the edges on an insert and across inserts in a batch of tools can be as high as 25 μm (0.001 in). Statistically significant variations are also seen in the corner radius region in which much cutting occurs in turning, boring and face milling processes. Orthogonal cutting tests with tools of measured edge radius in the zone of cut indicate that the machining forces, especially the thrust force component, are sensitive to changes in edge radius on the order of measured variations. [S1087-1357(00)01603-8]

Introduction

Edge hones are commonly used as an edge preparation in many operations, like interrupted cutting, machining of hard materials, etc., where increased edge strength is desired. Edge hones in the

[1]Currently with General Motors.
[2]Currently with Lamb Technicon Machining Systems, Warren, MI.

Contributed by the Manufacturing Engineering Division for publication in the JOURNAL OF MANUFACTURING SCIENCE AND ENGINEERING. Manuscript received July 1997; revised Oct. 1999. Associate Technical Editor: S. Kapoor.

range of 75 μm (0.003 in) to 125 μm (0.005 in) are commercially available for heavy duty machining of hardened steels (>35 Rc) and cast irons. The edge preparations on commercially available inserts are generally prescribed as a range. For example, edge preparation *A* is specified to have a hone ranging from 10 μm (0.0005 in) to 80 μm (0.003 in). Two of the processes that are commonly used to obtain edge hones are honing by nylon brushes impregnated with silicon carbide, and honing by abrasive entrainment in an air-stream. In the brush honing process considered here, cutting edges are polished when the inserts, mounted on a rotary carrier, are slowly rotated about their inscribed-circle axis while being fed through the rotating brushes. By varying the time and depth of contact between the brush and the cutting edge, different edge hones can be obtained. The variation of an edge feature from its nominal value, both along an edge and edge-to-edge, is not well understood. Large tolerances on the edge hone could lead to significant variations in machining forces when cutting with different inserts of the same nominal specification. The aim of the reported work is to study edge hone variability on commercial inserts and the relative effects on machining forces and model calibration data. It is *not* the aim of this paper to *model* the effects of the edge radius on the cutting process, nor is it to model the brush honing process.

Edge Radius Measurements

Accurate measurement of the edge radius is a fairly difficult task that has been addressed in some detail in only a few studies [1,2]. In this study, we describe the use of a new optical technique based on white light interferometry (see Sasmor and Caber [3] for a detailed review of optical measurement techniques). The WYKO™ measurement system used here, which is based on the physics of white light phase-shift interferometry, combines accurate optics, axis movement and a computational software interface to make measurements with vertical resolution as good as 2 nm (0.002 μm) [4].

Three sets of TPG432 uncoated carbide inserts (sets *A*, *B* and *C*) were requested from a vendor to have corresponding nominal edge radii (specified at the center of the edge) of 50.8 μm (0.002 in), 100.6 μm (0.004 in) and 152.4 μm (0.006 in). After going through quality checks at the vendor's facility, the inserts were measured independently by the research team. Care was taken to reduce sources of measurement errors. A small fixture that held the insert at the proper (and constant) orientation relative to the optics of the system, together with an automated positioning table, ensured that measurements on different inserts and edges were at identical locations along the edge. Repeatability tests showed that the estimated profiles were within 50 nm (0.05 μm) of each other. Details of scan data processing are given in [5].

Variability Between Edges and Inserts. Eight inserts from each set were chosen to evaluate the variability across edges and inserts. Comparing the nominal specifications to the measured data indicated that the edge-center-point means were smaller than the prescribed nominal values, in this case by about 15 μm (0.0007 in) for the sets *A* and *B*, and by about 5 μm (0.0002 in) for set *C*. This would indicate that it is difficult to manufacture the inserts to a tight tolerance on the mean for tools with a smaller edge radius (within 35 percent of the nominal for set *A* as compared to within 3 percent for set *C*). The variation about the mean is about 6 μm (0.00025 in) for sets *A* and *B*, and 14 μm (0.0005 in) for set *C*, which is approximately 10 percent of the nominal values for all sets. Only 50 percent of the measured values were in a range of 10 μm (0.0004 in) for sets *A* and *B*, and 25 μm (0.001 in) for set *C*.

A general nested linear analysis of variance was conducted in which the edge radius was modeled as equal to a tool effect plus a nested effect of edge on tool. It was found that both these variables were statistically significant at a *P*-level of 0.024 on tool and 0.014 on edge (both of set *B*). Sets *A* and *C* were significant at even smaller *P*-values. In other words, between inserts there existed a significant shift in insert mean (the average of the edge-center-point measurements on each of the three edges of an insert) and, furthermore, there existed an edge-to-edge mean shift on each insert.

Placing 95 percent confidence bands on the insert means for nine inserts of set *A* demonstrated that if an insert with nominal edge radius of 50.8 μm (0.002 in) is procured commercially, the actual edge radius at a specified point on the edge could be off by as much as 22 μm (0.0009 in). This error is perhaps indicative of why most manufacturers specify the edge preparations in ranges of values.

Variability Along an Edge. The second important issue to investigate is whether or not the location along the cutting edge affects the edge radius in a statistically significant manner. Two inserts from every set were chosen and measurements were made on four of the six edges at five zones on each edge corresponding to 7.8 mm, 5.2 mm, 0.7 mm, −3.4 mm and −6.7 mm from the center of the edge. These points were chosen such that one point corresponded approximately to the center of the edge with the other points distributed on either side. Using the automated positioning table, the locations of these positions were maintained to be the same for all the measured edges. The variation of edge radius along the edge is shown in Fig. 1. It is obvious that the edge radius at the center of the edge is consistently lower as compared to the radius at points closer to the corner (7.8 mm and −6.7 mm locations). The R^2 values for the individual fits were about 60 percent. Analysis of variance showed that edge location indeed was a significant factor. It also showed that the edge-number label was insignificant.

Variability Around Insert Corner. While variability along the straight portion of an insert edge may impact straight-edged orthogonal cutting tests, most real-world applications of cutting inserts involve cutting, at least in part, on the corner radius of the insert. Therefore, force prediction models being developed for such applications, which extend the models being formulated for straight-edged orthogonal cutting, should account for edge radius variation around the corner, if it exists. With this in mind, the edge radius around the corner was measured on several inserts from set *A* to evaluate the relative variation in the corner region as compared to the straight lead-edge region studied above.

A fixture was fabricated to permit three measurements on each corner—one at each of the two tangent points where the corner meets the two straight edges, and one at the apex of the corner. The statistical model employed to analyze these data was a general linear model with the corners as nested within insert for the same reason edge number was nested within insert in the earlier analysis. The two possible two-factor interactions were also

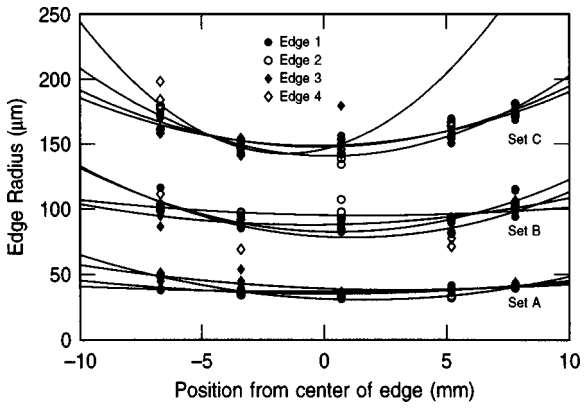

Fig. 1 The variation of edge radius along the four cutting edges of inserts from set *A* (50.8 μm (0.002 in)), set *B* (101.6 μm (0.004 in)), and set *C* (152.4 μm (0.006 in))

evaluated in this model. Results of the statistical evaluation show insert and position to be statistically significant, at *P*-values of 0.035 and 0.009, respectively, and corner(insert) as well as the two interactions to be insignificant. This reveals that the edge radius does vary with position around any given corner and furthermore that there is a difference between inserts, although variation between corners of a single insert is statistically indistinguishable from random errors.

Force Measurement Considerations

Orthogonal cutting experiments were conducted on a J & L CNC lathe by end cutting of tubes of three materials: gray cast iron, 2024 aluminum and commercially pure zinc. A wall thickness equal to 4.83 mm (0.19 in) was used to maintain plane strain conditions. A Kistler piezoelectric dynamometer was used to monitor three machining force components. To reduce the variation of the edge radius along the width of cut, which could lead to misleading force measurements, all the cutting tests were performed at the center of the edge where the edge radius had been measured prior to the experiment and where the variation gradient is lowest across the width of cut. It can be seen from Fig. 1 that the maximum variation in edge radius across a 5 mm (0.2 in) width of cut that is equally distributed about the edge center-point is only about 6 μm (0.0004 in) for inserts from set *C*.

Each material was cut at several feeds by two inserts whose hones were described by the vendor as 50 μm (0.002 in) and 100 μm (0.004 in). Since the significance of the effect of the edge radius increases at smaller uncut chip thickness, feeds were selected such that the ratio of uncut chip thickness to edge radius (h/r_n) varied between 0.5 and 5. This represents the range commonly seen in the operations of practical interest (hard turning and finishing operations). The edge radius effects seen here would be more pronounced at even lower uncut chip thicknesses.

Graphs of the cutting and thrust forces (normalized by the width of cut) versus the uncut chip thickness *h*, for all three materials, are presented in Figs. 2 and 3. As expected, the effect of the edge radius is visibly larger on the thrust force than on the cutting force. It can be seen that intercepts (a qualitative measure of edge/ploughing contributions) are higher when the materials are being cut with tools of higher edge radius. Even for zinc where the edge radius effect seems to be quite small, 95 percent confidence bands on the force measurements lie far apart (band-to-band separation of 2.5 to 3 times the confidence bands), which statistically supports the significance of the edge radius effect on the forces. If it is assumed that there is a linear variation of machining forces with edge radius, then it can be shown that the predicted force for an insert with edge radius of 75.6 μm (0.003 in) would lie well between the confidence bands of sets *A* and *B*.

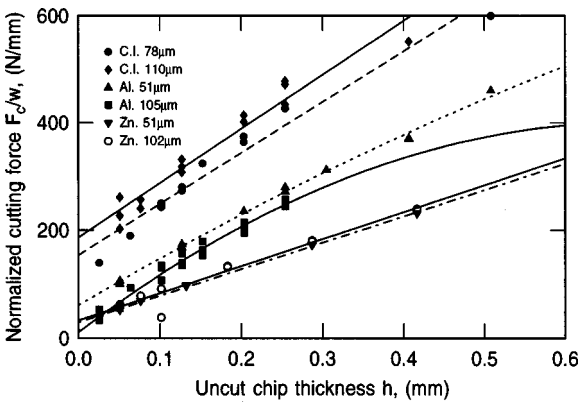

Fig. 2 Variation of the cutting force component with uncut chip thickness for cast iron, aluminum and zinc at various edge radii

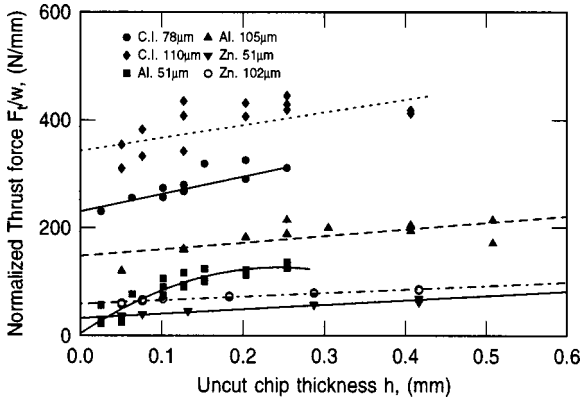

Fig. 3 Variation of the thrust force component with uncut chip thickness for cast iron, aluminum and zinc at various edge radii

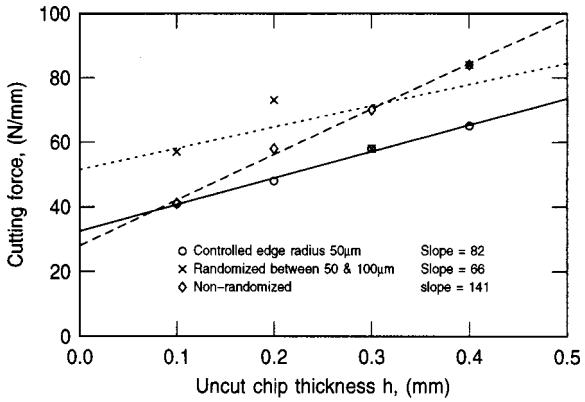

Fig. 4 Increased errors observed when different parts of the cutting edge are used for calibration testing

This proves that the increase in forces are of a higher order than the experimental error in the force measurements.

The variability along an edge raises an important consequence regarding force measurements made for force model calibration via straight-edged orthogonal cutting tests. If the machining forces are assumed to have some portion that is proportional to the edge radius, then the machining force must vary parabolically along the length of the cutting edge. Arbitrary or randomized selection of zones along the cutting edge will result in measurement of machining forces that appear to exhibit noise. Machining force data is meaningful only when all the tests are run with tools of the same edge radius. In Fig. 4, cutting forces that were predicted using a simple force model, based on data collected here, are shown for three situations—controlled tests in which a single edge radius is used, randomized tests along the cutting edge, and non-randomized tests. It can be seen that randomized and nonrandomized tests lead to lower R^2 values and, more importantly, an incorrect slope and/or intercept. Hence, we can conclusively state that it is important to measure and maintain the edge radius at the cutting zone in order to obtain accurate force data.

Conclusions

It was shown that there is a statistically significant parabolic variation of edge radius along a cutting edge, which is presumably due to the geometry of the brush honing process. Statistically significant variation of the edge-center-point mean across edges and inserts (about 25 μm) was also observed, which is attributed to the difficulty of controlling the honing process. Variation was observed in the corner radius region as well, being statistically

significant around the corner and from insert to insert. It was also shown that the machining force components are sensitive to changes in edge radius on the order of the measured edge variation. This machining force sensitivity is of a higher order than experimental error (noise) in the measurement of forces. Hence, accurate prediction of force magnitude and direction, for honed tools, may likely require consideration of hone variation around the corner and along the lead edge. Furthermore, care must be taken to avoid introducing hone variation by changing edges or adjusting the cutting-zone location along the edge when conducting cutting tests, which is a typical approach to avoiding excessive wear evolution over the duration of a set of tests.

This study also further supports the fact that edge radius plays an important role in process mechanics, particularly at conditions of low h/r_n. Work that addresses the effects of the edge radius on the cutting process and the development of a cutting model that alleviates the sharp tool assumption are in progress.

Acknowledgments

The authors would like to thank Mr. Glenn Novak of the Polymers Department, General Motors Research Center, for the use of the measurement system. We also thank Dr. Don Cohen of Michigan Metrology for his help in optimizing the system for our use.

References

[1] Albrecht, P., 1960, ''New developments in the theory of metal cutting process,'' J. Eng. Ind., **82**, pp. 348–358.
[2] Nakayama, K., and Tamura, K., 1968, ''Size effect in metal cutting force,'' J. Eng. Ind., **90**, pp. 119–126.
[3] Sasmor, J., and Caber, P., 1996, ''Interferometer—Handles the rough jobs,'' Photonics Spectra, **30**, pp. 93–98.
[4] Caber, P. J., 1993, ''Interferometric profiler for rough surfaces,'' Appl. Opt., **32**, pp. 3438–3441.
[5] Schimmel, R. S., Manjunathaiah, J., and Endres, W. J., 1997, ''An experimental investigation of the variability of edge hones and their effects on machining forces,'' G. J. Weins, ed., Manufact. Sci. Eng., MED **6-2**, pp. 261–268.